Durelli, L., Conti, L., Clerico, M., Boselli, D., Contessa, G., Ripellino, P., Ferrero, B., Eid, P., Novelli, F., 2009. T-helper 17 cells expand in multiple sclerosis and are inhibited by interferon-beta. Ann. Neurol. 65, 499–509.
Floris, S., Ruuls, S.R., Wierinckx, A., Van Der Pol, S.M., Dopp, E., Van Der Meide, P.H., Dijkstra, C.D., De Vries, H.E., 2002. Interferon-beta directly influences monocyte infiltration into the central nervous system. J. Neuroimmunol. 127, 69–79.
Goverman, J., 2009. Autoimmune T cell responses in the central nervous system. Nat. Rev. Immunol. 9, 393–407.
Guo, B., Chang, E.Y., Cheng, G., 2008. The type I IFN induction pathway constrains Th17-mediated autoimmune inflammation in mice. J. Clin. Invest. 118, 1680–1690.
Inoue, M., Williams, K.L., Oliver, T., Vandenabeele, P., Rajan, J.V., Miao, E.A., Shinohara, M.L., 2012. Interferon-beta therapy against EAE is effective only when development of the disease depends on the NLRP3 inflammasome. Sci. Signal. 5, ra38.
Ishizu, T., Osoegawa, M., Mei, F.J., Kikuchi, H., Tanaka, M., Takakura, Y., Minohara, M., Murai, H., Mihara, F., Taniwaki, T., Kira, J., 2005. Intrathecal activation of the IL-17/IL-8 axis in opticospinal multiple sclerosis. Brain 128, 988–1002.
Ivanov, Ii, Mckenzie, B.S., Zhou, L., Tadokoro, C.E., Lepelley, A., Lafaille, J.J., Cua, D.J., Littman, D.R., 2006. The orphan nuclear receptor RORgammat directs the differentiation program of proinflammatory IL-17+ T helper cells. Cell 126, 1121–1133.
Jiang, H., Milo, R., Swoveland, P., Johnson, K.P., Panitch, H., Dhib-Jalbut, S., 1995. Interferon beta-1b reduces interferon gamma-induced antigen-presenting capacity of human glial and B cells. J. Neuroimmunol. 61, 17–25.
Kappos, L., Freedman, M.S., Polman, C.H., Edan, G., Hartung, H.-P., Miller, D.H., Montalbán, X., Barkhof, F., Radü, E.-W., Bauer, L., Dahms, S., Lanius, V., Pohl, C., Sandbrink, R., 2007. Effect of early versus delayed interferon beta-1b treatment on disability after a first clinical event suggestive of multiple sclerosis: a 3-year follow-up analysis of the BENEFIT study. Lancet 370, 389–397.
Kieseier, B.C., 2011. The mechanism of action of interferon-beta in relapsing multiple sclerosis. CNS Drugs 25, 491–502.
Kimura, A., Naka, T., Kishimoto, T., 2007. IL-6-dependent and -independent pathways in the development of interleukin 17-producing T helper cells. Proc. Natl. Acad. Sci. U. S. A. 104, 12099–12104.
Kozovska, M.E., Hong, J., Zang, Y.C., Li, S., Rivera, V.M., Killian, J.M., Zhang, J.Z., 1999. Interferon beta induces T-helper 2 immune deviation in MS. Neurology 53, 1692–1697.
Kumanogoh, A., Marukawa, S., Suzuki, K., Takegahara, N., Watanabe, C., Ch'ng, E., Ishida, I., Fujimura, H., Sakoda, S., Yoshida, K., Kikutani, H., 2002. Class IV semaphorin Sema4A enhances T-cell activation and interacts with Tim-2. Nature 419, 629–633.
Kumanogoh, A., Shikina, T., Suzuki, K., Uematsu, S., Yukawa, K., Kashiwamura, S., Tsutsui, H., Yamamoto, M., Takamatsu, H., Ko-Mitamura, E.P., Takegahara, N., Marukawa, S., Ishida, I., Morishita, H., Prasad, D.V., Tamura, M., Mizui, M., Toyofuku, T., Akira, S., Takeda, K., Okabe, M., Kikutani, H., 2005. Nonredundant roles of Sema4A in the immune system: defective T cell priming and Th1/Th2 regulation in Sema4A-deficient mice. Immunity 22, 305–316.
Lee, L.F., Axtell, R., Tu, G.H., Logronio, K., Dilley, J., Yu, J., Rickert, M., Han, B., Evering, W., Walker, M.G., Shi, J., De Jong, B.A., Killestein, J., Polman, C.H., Steinman, L., Lin, J.C., 2011. IL-7 promotes T(H)1 development and serum IL-7 predicts clinical response to interferon-beta in multiple sclerosis. Sci. Transl. Med. 3, 93ra68.
Mcrae, B.L., Semnani, R.T., Hayes, M.P., Van Seventer, G.A., 1998. Type I IFNs inhibit human dendritic cell IL-12 production and Th1 cell development. J. Immunol. 160, 4298–4304.
Meda, C., Molla, F., De Pizzol, M., Regano, D., Maione, F., Capano, S., Locati, M., Mantovani, A., Latini, R., Bussolino, F., Giraudo, E., 2012. Semaphorin 4A exerts a proangiogenic effect by enhancing vascular endothelial growth factor-A expression in macrophages. J. Immunol. 188, 4081–4092.
Nagai, T., Devergne, O., Mueller, T.F., Perkins, D.L., Van Seventer, J.M., Van Seventer, G.A., 2003. Timing of IFN-beta exposure during human dendritic cell maturation and naive Th cell stimulation has contrasting effects on Th1 subset generation: a role for IFN-beta-mediated regulation of IL-12 family cytokines and IL-18 in naive Th cell differentiation. J. Immunol. 171, 5233–5243.
Nakatsuji, Y., Nakano, M., Moriya, M., Kishigami, H., Tatsumi, C., Tada, S., Sadahiro, S., Naka, T., Mitani, K., Funauchi, M., Azuma, T., Watanabe, S., Kinoshita, M., Kajiyama, K., Yuasa, Y., Kaido, M., Takahashi, M.P., Naba, I., Hazama, T., Sakoda, S., 2006. Beneficial effect of interferon-beta treatment in patients with multiple sclerosis is associated with transient increase in serum IL-6 level in response to interferon-beta injection. Cytokine 36, 69–74.
Nakatsuji, Y., Okuno, T., Moriya, M., Sugimoto, T., Kinoshita, M., Takamatsu, H., Nojima, S., Kimura, T., Kang, S., Ito, D., Nakagawa, Y., Toyofuku, T., Takata, K., Nakano, M., Kubo, M., Suzuki, S., Matsui-Hasumi, A., Uto-Konomi, A., Ogata, A., Mochizuki, H., Sakoda, S., Kumanogoh, A., 2012. Elevation of Sema4A implicates Th cell skewing and the efficacy of IFN-beta therapy in multiple sclerosis. J. Immunol. 188, 4858–4865.
Noseworthy, J.H., Lucchinetti, C., Rodriguez, M., Weinshenker, B.G., 2000. Multiple sclerosis. N. Engl. J. Med. 343, 938–952.
Okuda, Y., Okuda, M., Bernard, C.C.A., 2002. Gender does not influence the susceptibility of C57BL/6 mice to develop chronic experimental autoimmune encephalomyelitis induced by myelin oligodendrocyte glycoprotein. Immunol. Lett. 81, 25–29.
Palmer, A.M., 2013. Multiple sclerosis and the blood–central nervous system barrier. Cardiovasc. Psychiatry Neurol. 2013, 530356.
Pelletier, D., Hafler, D.A., 2012. Fingolimod for multiple sclerosis. N. Engl. J. Med. 366, 339–347.
Ramgolam, V.S., Sha, Y., Jin, J., Zhang, X., Markovic-Plese, S., 2009. IFN-beta inhibits human Th17 cell differentiation. J. Immunol. 183, 5418–5427.
Ransohoff, R.M., 2007. Natalizumab for multiple sclerosis. N. Engl. J. Med. 356, 2622–2629.
Rio, J., Nos, C., Tintore, M., Tellez, N., Galan, I., Pelayo, R., Comabella, M., Montalban, X., 2006. Defining the response to interferon-beta in relapsing-remitting multiple sclerosis patients. Ann. Neurol. 59, 344–352.
Rudick, R.A., Goelz, S.E., 2011. Beta-interferon for multiple sclerosis. Exp. Cell Res. 317, 1301–1311.
Sempere, A.P., Berenguer-Ruiz, L., Khabbaz, E., 2013. Oral BG-12 in multiple sclerosis. N. Engl. J. Med. 368, 1652.
Shimizu, J., Hatanaka, Y., Hasegawa, M., Iwata, A., Sugimoto, I., Date, H., Goto, J., Shimizu, T., Takatsu, M., Sakurai, Y., Nakase, H., Uesaka, Y., Hashida, H., Hashimoto, K., Komiya, T., Tsuji, S., 2010. IFNbeta-1b may severely exacerbate Japanese optic-spinal MS in neuromyelitis optica spectrum. Neurology 75, 1423–1427.
Takata, K., Kinoshita, M., Okuno, T., Moriya, M., Kohda, T., Honorat, J.A., Sugimoto, T., Kumanogoh, A., Kayama, H., Takeda, K., Sakoda, S., Nakatsuji, Y., 2011. The lactic acid bacterium Pediococcus acidilactici suppresses autoimmune encephalomyelitis by inducing IL-10-producing regulatory T cells. PLoS One 6, e27644.
Toyofuku, T., Yabuki, M., Kamei, J., Kamei, M., Makino, N., Kumanogoh, A., Hori, M., 2007. Semaphorin-4A, an activator for T-cell-mediated immunity, suppresses angiogenesis via Plexin-D1. EMBO J. 26, 1373–1384.
Zhang, L., Yuan, S., Cheng, G., Guo, B., 2011. Type I IFN promotes IL-10 production from T cells to suppress Th17 cells and Th17-associated autoimmune inflammation. PLoS One 6, e28432.

Ultra-low-dose CT of the Lung:

Effect of Iterative Reconstruction Techniques on Image Quality

Masahiro Yanagawa, MD, PhD, Tomoko Gyobu, MD, Ann N. Leung, MD, Misa Kawai, MD, Yutaka Kawata, MD, Hiromitsu Sumikawa, MD, PhD, Osamu Honda, MD, PhD, Noriyuki Tomiyama, MD, PhD

Rationale and Objectives: To compare quality of ultra-low-dose thin-section computed tomography (CT) images of the lung reconstructed using model-based iterative reconstruction (MBIR) and adaptive statistical iterative reconstruction (ASIR) to filtered back projection (FBP) and to determine the minimum tube current–time product on MBIR images by comparing to standard-dose FBP images.

Materials and Methods: Ten cadaveric lungs were scanned using 120 kVp and four different tube current–time products (8, 16, 32, and 80 mAs). Thin-section images were reconstructed using MBIR, three ASIR blends (30%, 60%, and 90%), and FBP. Using the 8-mAs data, side-to-side comparison of the four iterative reconstruction image sets to FBP was performed by two independent observers who evaluated normal and abnormal findings, subjective image noise, streak artifact, and overall image quality. Image noise was also measured quantitatively. Subsequently, 8-, 16-, and 32-mAs MBIR images were compared to standard-dose FBP images. Comparisons of image sets were analyzed using the Wilcoxon signed rank test with Bonferroni correction.

Results: At 8 mAs, MBIR images were significantly better ($P < .005$) than other reconstruction techniques except in evaluation of interlobular septal thickening. Each set of low-dose MBIR images had significantly lower ($P < .001$) subjective and objective noise and streak artifacts than standard-dose FBP images. Conspicuity and visibility of normal and abnormal findings were not significantly different between 16-mAs MBIR and 80-mAs FBP images except in identification of intralobular reticular opacities.

Conclusions: MBIR imaging shows higher overall quality with lower noise and streak artifacts than ASIR or FBP imaging, resulting in nearly 80% dose reduction without any degradations of overall image quality.

Key Words: Radiation dose reduction; model-based iterative reconstruction; adaptive statistical iterative reconstruction; filtered back projection; image quality.

The increase of the radiation dose delivered in computed tomography (CT) has recently been a problem. Because there is a trade-off between image quality and radiation dose on CT, however, it is not always appropriate to decrease radiation dose on CT. Iterative reconstruction algorithms for CT have been developed by multiple equipment manufacturers to reduce image noise associated with radiation dose reduction (1–8). Adaptive statistical iterative reconstruction (ASIR) and model-based iterative reconstruction (MBIR) are types of iterative reconstruction algorithms available on clinical settings. The ASIR technique models photon and electronic noise statistics; by partially correcting for fluctuations in projection measurements due to limited photon statistics, ASIR enables a time-efficient reduction in pixel variance that is statistically unlikely to be representative of anatomic features resulting in a reduction of image noise with no decrement in spatial resolution (9). In clinical practice, ASIR is typically used in combination with the standard filtered back projection (FBP) reconstruction to create blended images. As compared to ASIR, MBIR is a more mathematically complex and time-consuming technique as it models not only system statistics but also system optics (10). Phantom experiments show that MBIR has potential to improve spatial resolution and allow further reductions in image noise (9). To date, few studies have evaluated CT image quality of the lung using MBIR (10–14). Thus, unlike FBP and ASIR, MBIR technique might have the potential not to degrade image quality even under the extreme dose reduction. McCollough et al. (15) reported that the advances in data acquisition, image reconstruction, and optimization processes that were identified by consensus as being necessary to achieve submillisievert-dose CT examinations. It is expected that MBIR might be one of techniques to enable a submillisievert-dose CT. The present study was performed using cadaveric lung models that can provide multiple acquisitions to determine the minimum tube current–time product at which image quality of a low-dose MBIR study is comparable to that of a standard-dose FBP study. The aim of this present study was two-fold: to compare quality of ultra-low-dose

Acad Radiol 2014; 21:695–703

From the Department of Diagnostic Radiology, Stanford University School of Medicine, 1201 Welch Rd, Stanford, CA 94305 (M.Y., A.N.L.); Department of Radiology, Osaka University Graduate School of Medicine, Suita, Osaka, Japan (M.Y., T.G., M.K., H.S., O.H., N.T.); and Department of Radiology, Osaka Rosai Hospital, Sakai, Osaka, Japan (Y.K.). Received December 2, 2013; accepted January 31, 2014. All authors declare that there is no conflict of interest. **Address correspondence to:** M.Y. e-mail: masayana@stanford.edu or m-yanagawa@radiol.med.osaka-u.ac.jp

http://dx.doi.org/10.1016/j.acra.2014.01.023

thin-section CT images of the lung reconstructed using MBIR and ASIR to FBP and to determine the minimum tube current–time product at which image quality of an MBIR study is comparable to that of a standard-dose FBP.

MATERIALS AND METHODS

Cadaveric Lungs and Imaging

We obtained approval from our internal Ethics Review Board. Informed consent was obtained for the use of patient biomaterial and for retrospective review of patient records and images. Ten cadaveric lungs were inflated and fixed by the method of Heitzman (16). These lungs were distended through the main bronchus with fixative fluid that contained polyethylene glycol 400, 95% ethyl alcohol, 40% formalin, and water in the proportions of 10:5:2:3. The specimens were immersed in fixative for 2 days and the lungs were then air dried. The pathologic diagnoses of these 10 lungs were usual interstitial pneumonia (n = 1), diffuse alveolar damage (n = 1), diffuse panbronchiolitis (n = 1), pneumonia (n = 2), emphysema (n = 1), diffuse alveolar hemorrhage (n = 1), metastatic disease (n = 2), and lymphangitic carcinomatosis (n = 1).

The 10 lungs were scanned on an multi-detector row CT (MDCT) scanner (Discovery CT750HD; GE Healthcare Technologies, Milwaukee, WI). CT protocol was as follows: detector collimation, 0.625 mm; detector pitch, 0.984; gantry rotation period, 0.4 seconds; matrix size, 512 × 512 pixels; 30-cm scan length; x-ray voltage, 120 kVp; tube current, 20, 40, 80, and 200 mA; and non–high-resolution mode with 984 views per rotation. Both ASIR and MBIR are part of the commercially available package implemented on the control panel of the CT scanner.

Axial thin-section CT images of 0.625 mm thickness and 20 cm field of view were reconstructed with MBIR, ASIR (30%, 60%, and 90% [represented as $ASIR_{30}$, $ASIR_{60}$, and $ASIR_{90}$]), and FBP. The voxel dimensions of CT image are 0.391 × 0.391 × 0.625 mm. A high–spatial-frequency algorithm was used in ASIR and FBP; however, there was no concept of reconstruction algorithm in MBIR. Based on lung cancer screening literature (17) that defines a tube current–time product of 40 mAs as "low dose", we use the term "ultra-low-dose" CT to refer to studies acquired with tube current–time products ≤20 mAs and result in an effective dose of <1 mSv.

Subjective Image Analysis

Three to four cross-sectional levels with the most conspicuous CT findings were chosen from each cadaveric lung by the principal investigator (M.Y., with 12 years of experience): three images were selected for seven lungs and four images for the remaining three lungs. There were a total of 264 images, that is, 33 sets of 8 image series (8-mAs, 16-mAs, and 32-mAs MBIR, 8-mAs $ASIR_{30}$, 8-mAs $ASIR_{60}$, 8-mAs $ASIR_{90}$, and 8-mAs and 80-mAs FBP).

TABLE 1. Radiation Dose Descriptions

	Low Dose			Standard Dose
	8 mAs	16 mAs	32 mAs	80 mAs
CTDIvol (mGy)	0.65	1.30	2.59	6.49
DLP (mGy-cm)	22.15	44.30	88.60	221.50
ED (mSv)	0.31	0.62	1.24	3.10

CTDIvol, computed tomography dose index volume; DLP, dose-length product; ED, effective dose.

Two independent chest radiologists (M.K. and Y.K., with 8 years of experience each) without prior knowledge of the pathologic diagnoses, image acquisition parameters, or iterative reconstruction techniques reviewed the 264 images on a 5-megapixel 21-in monochrome liquid-crystal display monitor. All images were displayed at a window level of −700 Hounsfield units (HU) and a window width of 1200 HU. In the first step, 8-mAs MBIR and 8-mAs ASIR were compared to 8-mAs FBP. Approximately 1 month later, in the second step, 8-mAs, 16-mAs, and 32-mAs MBIR were compared to 80-mAs FBP.

The two observers compared the conspicuity and visibility of normal (central and peripheral vessels, central and peripheral airways, and interlobar fissures) and abnormal (ground-glass opacity [GGO], consolidation, nodules, interlobular septal thickening, intralobular reticulation, cyst, and bronchiectasis) CT findings using a five-point scale as compared to the FBP image: (1) an unacceptable image on which it was more difficult to detect and/or visualize findings in whole lung; (2) an inferior image on which it was more difficult to detect and/or visualize findings in at least one area of the lung; (3) an image comparable to the FBP image; (4) a superior image on which it was easier to detect and/or visualize findings in at least one area of the lung; and (5) an excellent image on which it was easier to detect and/or visualize findings in whole lung. Subjective visual noise and streak artifact were also graded on a five-point comparative scale: (1) noise/artifact significantly worse, nondiagnostic; (2) noise/artifact worse; (3) similar noise/artifact compared to image of FBP; (4) noise/artifact improved; and (5) noise/artifact significantly improved, almost nondetectable. Overall image quality was finally graded on a five-point scale: (1) unacceptable, nondiagnostic; (2) inferior; (3) comparable to the FBP image; (4) better; and (5) excellent. If there were different scores between two observers, final evaluation was decided by an adjudicator (H.S., with 13 years of experience).

Objective Image Analysis

Quantitative noise measurements were calculated by measuring the standard deviation (SD) in a circular region of interest (ROI) defined by an electric cursor, using free software (ImageJ version 1.37v; NIH, Bethesda, MD; for further information regarding ImageJ software, see http://rsb.info.nih.gov/ij/index.html). Quantitative noise measurements

TABLE 2. Comparison among FBP, ASIR, and MBIR on Ultra-low-dose (8 mAs) CT

	Normal Findings			Abnormal Findings			Other Findings		Overall Image Quality
	Central Vessels and Airways	Peripheral Vessels and Airways	Interlobar Fissures	Nodules	GGO	ISP	Image Noise	Streak Artifact	
Reconstruction technique									
MBIR	4.83 ± 0.07	4.68 ± 0.09	4.75 ± 0.11	4.96 ± 0.04	4.84 ± 0.07	4.19 ± 0.16	5.00 ± 0.00	5.00 ± 0.00	4.97 ± 0.03
$ASIR_{90}$	4.06 ± 0.11	4.04 ± 0.07	4.00 ± 0.13	4.00 ± 0.05	4.16 ± 0.07	3.88 ± 0.09	4.21 ± 0.07	4.03 ± 0.12	4.55 ± 0.09
$ASIR_{60}$	3.52 ± 0.09	3.32 ± 0.09	3.19 ± 0.10	3.39 ± 0.09	3.84 ± 0.07	3.31 ± 0.12	3.73 ± 0.08	3.45 ± 0.09	3.55 ± 0.09
$ASIR_{30}$	3.00 ± 0.00	3.00 ± 0.00	3.00 ± 0.00	3.04 ± 0.04	3.04 ± 0.04	3.00 ± 0.00	3.03 ± 0.03	3.00 ± 0.00	3.00 ± 0.00
FBP	3.00 ± 0.00	3.00 ± 0.00	3.00 ± 0.00	3.00 ± 0.00	3.00 ± 0.00	3.00 ± 0.00	3.00 ± 0.00	3.00 ± 0.00	3.00 ± 0.00
Pairwise comparison (*P**)									
MBIR versus $ASIR_{90}$	<.001	<.001	.005	<.001	<.001	.962	<.001	<.001	<.001
$ASIR_{60}$	<.001	<.001	<.001	<.001	<.001	.002	<.001	<.001	<.001
$ASIR_{30}$	<.001	<.001	<.001	<.001	<.001	<.001	<.001	<.001	<.001
FBP	<.001	<.001	<.001	<.001	<.001	<.001	<.001	<.001	<.001
$ASIR_{90}$ versus $ASIR_{60}$	<.001	<.001	<.001	<.001	.084	.005	<.001	<.001	<.001
$ASIR_{30}$	<.001	<.001	<.001	<.001	<.001	<.001	<.001	<.001	<.001
FBP	<.001	<.001	<.001	<.001	<.001	<.001	<.001	<.001	<.001
$ASIR_{60}$ versus $ASIR_{30}$	<.001	.026	.825	.006	<.001	.197	<.001	<.001	<.001
FBP	<.001	.026	.825	.003	<.001	.197	<.001	<.001	<.001
$ASIR_{30}$ versus FBP	1.000	1.000	1.000	1.000	1.000	1.000	1.000	1.000	1.000

ASIR, adaptive statistical iterative reconstruction; GGO, ground-glass opacity; ISP, interlobular septal thickening; FBP, filtered back projection; MBIR, model-based iterative reconstruction.

Data are presented as mean ± standard deviation. Data of the subjective image analysis were statistically analyzed using the Wilcoxon signed rank tests with a Bonferroni correction applied for multiple comparisons. *P** is a Bonferroni-corrected *P* value. *P** value <.05 was considered to be significant.

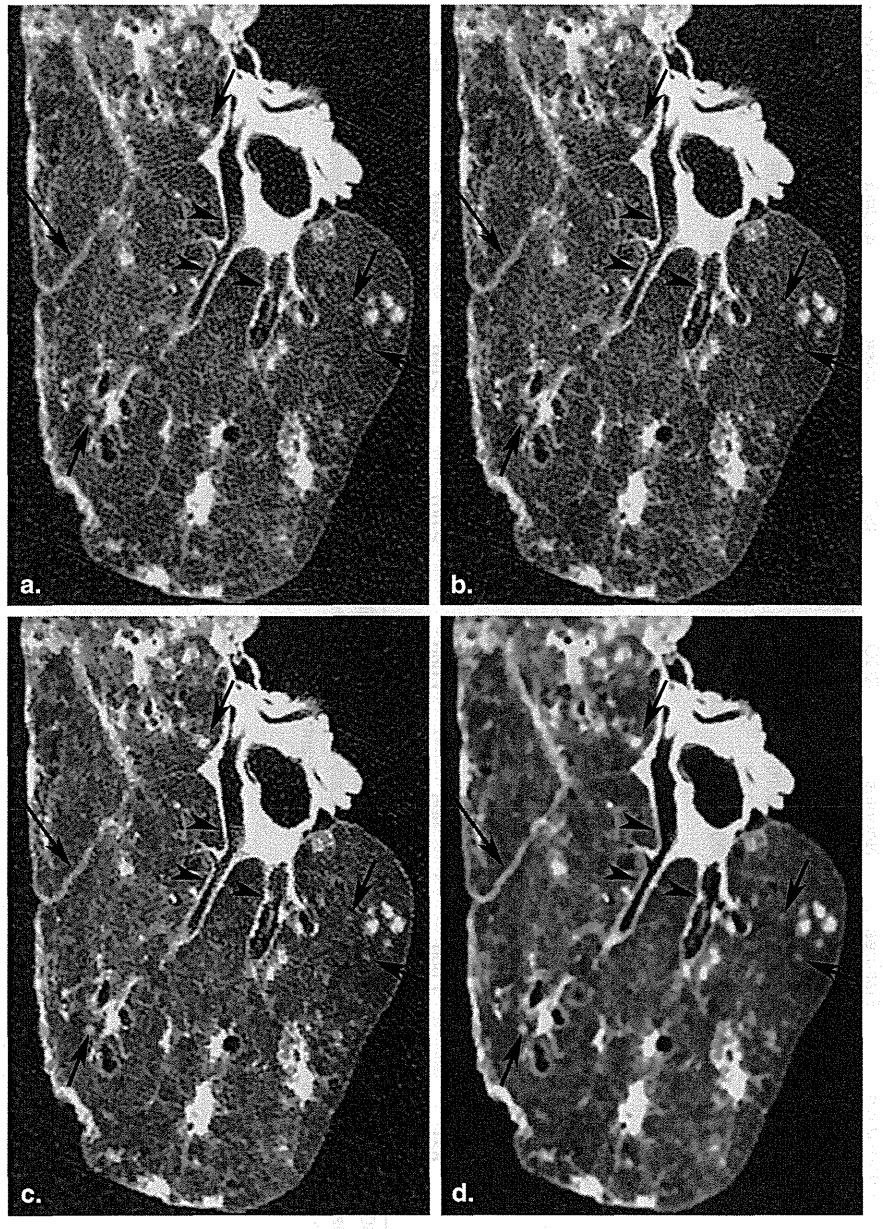

Figure 1. Ultra-low-dose (8 mAs) thin-section computed tomographic images of a cadaveric lung with diffuse panbronchiolitis show serial improvement in image noise and streak artifacts in following ascending order: FBP **(a)**, $ASIR_{30}$ **(b)**, $ASIR_{90}$ **(c)**, and MBIR **(d)**. With almost no perceptible noise or streak artifact on MBIR image, conspicuity and visibility of the fissure (*long arrow*), small nodules (*short arrows*), and bronchial walls (*arrowheads*) are improved as compared to FBP or ASIR blends. Note the blotchy pixilated appearance of the MBIR images. ASIR, adaptive statistical iterative reconstruction; FBP, filtered back projection; MBIR, model-based iterative reconstruction.

were obtained in the air adjacent to the lung specimen (18,19). An ROI (200 mm^2) was placed in four homogeneous parts of an image and was confirmed to be in exactly the same location on each image of a series by a collaborator (T.G., with 8 years of experience). Average values of SD were analyzed statistically.

Statistical Analysis

All statistical analyses were performed using commercially available software (MedCalc version 12.3.0.0 statistical software; Frank Schoonjans, Mariakerke, Belgium). Agreement between two observers in each evaluated category of CT findings was evaluated using the κ statistic and classified as poor (κ = 0.00–0.20), fair (κ = 0.21–0.40), moderate (κ = 0.41–0.60), good (κ = 0.61–0.80), or excellent (κ = 0.81–1.00). Data of the subjective image analysis were statistically analyzed using the Wilcoxon signed rank tests, which was conducted with Bonferroni correction applied for multiple comparisons. On the other hand, data of the objective image analysis were statistically analyzed using repeated measures analysis of variance pairwise comparison methods (Student's paired *t* test) with Bonferroni correction. A Bonferroni-corrected *P* value of <0.05 was considered significant.

RESULTS

Radiation Doses

Radiation dose measurements associated with low-dose (8, 16, and 32 mAs) and standard-dose (80 mAs) techniques

TABLE 3. Comparison between 8-mAs, 16-mAs, and 32-mAs MBIR Versus 80-mAs FBP

	Normal Findings			Abnormal Findings			Other Findings		Overall Image Quality
	Central Vessels and Airways	Peripheral Vessels and Airways	Interlobar Fissures	Nodules	GGO	ISP	Image Noise	Streak Artifact	
Reconstruction technique									
32-mAs MBIR	3.33 ± 0.09	3.50 ± 0.11	3.53 ± 0.17	3.46 ± 0.09	3.77 ± 0.11	3.44 ± 0.13	4.97 ± 0.03	4.97 ± 0.03	3.67 ± 0.12
16-mAs-MBIR	3.07 ± 0.07	3.14 ± 0.14	3.27 ± 0.12	3.18 ± 0.10	3.27 ± 0.13	2.75 ± 0.17	4.93 ± 0.05	4.93 ± 0.05	2.93 ± 0.08
8-mAs MBIR	3.07 ± 0.07	2.73 ± 0.18	2.93 ± 0.07	2.82 ± 0.12	2.86 ± 0.12	2.19 ± 0.10	4.87 ± 0.06	4.93 ± 0.05	2.63 ± 0.10
80-mAs FBP	3.00 ± 0.00	3.00 ± 0.00	3.00 ± 0.00	3.00 ± 0.00	3.00 ± 0.00	3.00 ± 0.00	3.00 ± 0.00	3.00 ± 0.00	3.00 ± 0.00
Pairwise comparison (*P**)									
32-mAs MBIR versus 16-mAs MBIR	.179	.047	.243	.108	.005	.002	1.000	1.000	<.001
8-mAs MBIR	.179	<.001	.015	.001	<.001	<.001	1.000	1.000	<.001
80-mAs FBP	.004	.001	.037	<.001	<.001	.023	<.001	<.001	<.001
16-mAs MBIR versus 8-mAs MBIR	1.000	.023	.115	.013	.023	.017	.965	1.000	.028
80-mAs FBP	1.000	1.000	.243	.576	.333	.983	<.001	<.001	1.000
8-mAs MBIR versus 80-mAs FBP	1.000	.821	1.000	.805	1.000	<.001	<.001	<.001	.007

ASIR, adaptive statistical iterative reconstruction; GGO, ground-glass opacity; ISP, interlobular septal thickening; FBP, filtered back projection; MBIR, model-based iterative reconstruction.
Data are presented as mean ± standard deviation. Data of the subjective image analysis were statistically analyzed using the Wilcoxon signed rank tests with a Bonferroni correction applied for multiple comparisons. *P** is a Bonferroni-corrected *P* value. *P** value <0.05 was considered to be significant.

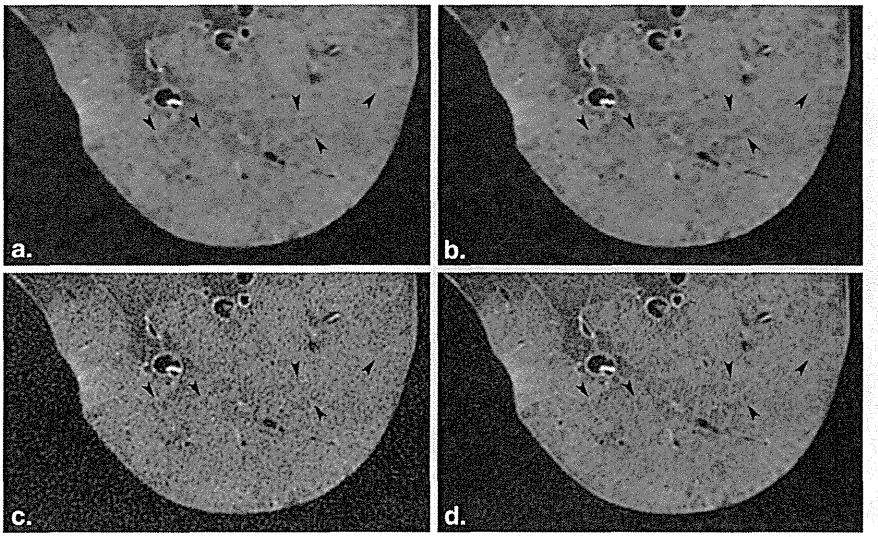

Figure 2. Thin-section computed tomographic images of a cadaveric lung with diffuse alveolar hemorrhage show diminished visibility of intralobular reticular opacities (*arrowheads*) on **(a)** 8-mAs and **(b)** 16-mAs MBIR images as compared to **(c)** 8-mAs and **(d)** 80-mAs FBP despite their higher noise levels. FBP, filtered back projection; MBIR, model-based iterative reconstruction.

used in scanning of the 10 cadaveric lungs are summarized in Table 1. The reported radiation dose measurements consist of CT dose index volume (CTDIvol), dose–length product (DLP), and effective dose (ED) which was calculated as the product of DLP and 'κ' conversion coefficient (0.014 mSv/[mGy cm]) for chest CT (20). Compared to standard-dose (80 mAs) technique, there were 80% and 90% decreases in dose measurements for 16-mAs and 8-mAs acquisitions, respectively with effective doses in the submillisievert range (0.31 and 0.62).

Subjective Evaluation of CT Findings

Comparisons between images reconstructed using MBIR, ASIR blends, and FBP and acquired at 8 mAs are summarized in Table 2. Statistical analysis of four findings (consolidation, intralobular reticular opacities, cyst, and bronchiectasis) could not be performed because of their low prevalence (<2% of cases). Interobserver agreement for each evaluated category of CT findings was from moderate to excellent (κ = 0.46–1.00). There were no kappa values in the following eight items because all the same scores were graded by two observers: on MBIR images, other findings (image noise and streak artifact); on $ASIR_{30}$ images, normal findings (central vessels and airways, peripheral vessels and airways, and interlobar fissures), interlobular septal thickening, streak artifacts, and overall image quality. In each evaluated category of CT findings, MBIR scored highest with significant differences between MBIR, ASIR blends, and FBP except for interlobular septal thickening, which was not significantly different between MBIR and $ASIR_{90}$. $ASIR_{90}$ images scored significantly higher in each category than the two lower ASIR blends or FBP except for GGO, which was not statistically different from $ASIR_{60}$ (P = .084). Conspicuity and visibility of CT findings using $ASIR_{30}$ were equivalent to FBP (P = 1.000; Fig. 1). Scores for subjective image noise and streak artifact significantly improved with increasing blends of ASIR (P < .001).

Comparisons between low-dose MBIR and standard-dose FBP images are summarized in Table 3. Interobserver agreement for each evaluated category of CT findings was from moderate to excellent (κ = 0.42–0.83). In each evaluated category of CT findings, 32-mAs MBIR scored highest with significant improvements in finding conspicuity, image noise, streak artifact, and overall image quality as compared to FBP ($P \leq .037$). Comparisons between ultra-low-dose (8 and 16 mAs) MBIR and 80-mAs FBP showed no statistically significant difference in conspicuity or visibility of normal and abnormal CT findings with the exception of interlobular septal thickening which was less well visualized on 8-mAs MBIR than on FBP (P < .001). A decrease in conspicuity of intralobular reticular opacities was identified by both observers on ultra-low-dose MBIR (Fig. 2) although formal statistical analysis could not be performed because of low prevalence of this finding. Scores for subjective image noise and streak artifact significantly improved on 8-mAs and 16-mAs MBIR images as compared to standard-dose FBP (P < .001), but with no significant differences among the three different dose MBIR image sets. Overall image quality was equivalent for 16-mAs MBIR (P = 1.00; Fig. 3) but inferior for 8-mAs MBIR (P = .028) as compared to FBP.

Quantitative Image Noise Measurements

Figure 4 shows sequential and statistically significant decreases (P < .001) in objective image noise on 8-mAs images reconstructed with FBP, increasing blends of ASIR and MBIR. Figure 5 similarly shows sequential and statistically significant decreases (P < .001) in objective image noise on images acquired and reconstructed using 80-mAs FBP and 8-, 16-, and 32-mAs MBIR.

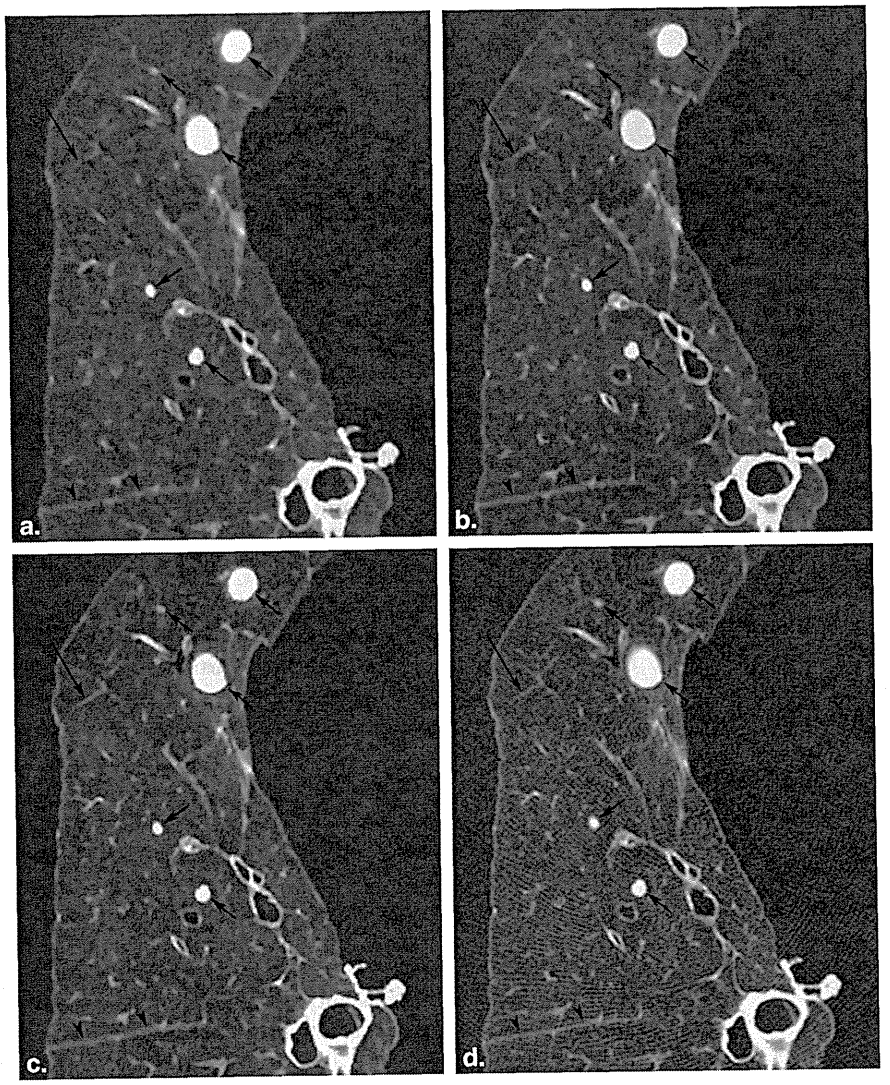

Figure 3. Thin-section computed tomographic images of a cadaveric lung with metastases acquired and reconstructed using 8-mAs MBIR **(a)**, 16-mAs MBIR **(b)**, 32-mAs MBIR **(c)**, and 80-mAs FBP **(d)** show similar low level of noise and streak artifacts on the three MBIR images, irrespective of dose. Conspicuity and visibility of peripheral vessels (*long arrow*), interlobar fissure (*arrowheads*), and margins of small and large nodules (*short arrows*) are worse on 8-mAs **(a)**, similar on 16-mAs **(b)**, and better on 32-mAs MBIR **(c)** images as compared to standard-dose FBP **(d)**. FBP, filtered back projection; MBIR, model-based iterative reconstruction.

DISCUSSION

The principle of ALARA (as low as reasonably achievable) urges radiologists to use the minimum level of radiation needed in imaging examinations to achieve the necessary diagnostic results. Iterative reconstruction algorithms are one of the newer options in the available dose reduction armamentarium that has included restriction of length of coverage, reduced tube voltage, and tube current modulation (11). Of the two iterative reconstruction algorithms evaluated in this study, ASIR, which was introduced earlier, has been more extensively studied (1–8,21–23) and has now largely been implemented into routine clinical practice. In comparison, MBIR, a more mathematically complex reconstruction technique, offers greater potential in dose reduction but at the cost of longer reconstruction times on the order of 45–60 minutes per series (10,11,24). Few studies to date (10–14) have evaluated image quality and diagnostic adequacy of ultra-low-dose MBIR for thin-section chest CT studies.

Our study showed that both ASIR and MBIR can improve lung image quality on ultra-low-dose CT as compared to FBP with MBIR images rated highest. These results are consistent with those of prior clinical studies (10,14) that have reported that when scanning at submillisievert doses, MBIR is superior to ASIR in generating diagnostically acceptable thin-section chest CT images largely because of marked reductions in image noise.

Of the four different iterative reconstructions performed in our study, overall image quality, image noise, and streak artifact were each rated best for MBIR and sequentially decreased with lower blends of ASIR ($ASIR_{90} > ASIR_{60} > ASIR_{30}$). Although a pixilated blotchy appearance has previously been described in association with high-percentage ASIR blends (6,22), this feature was not observed in this study likely related to interval improvements of the ASIR algorithm by the vendor (10). A blotchy appearance however was characteristic of MBIR images, which rendered blinding of

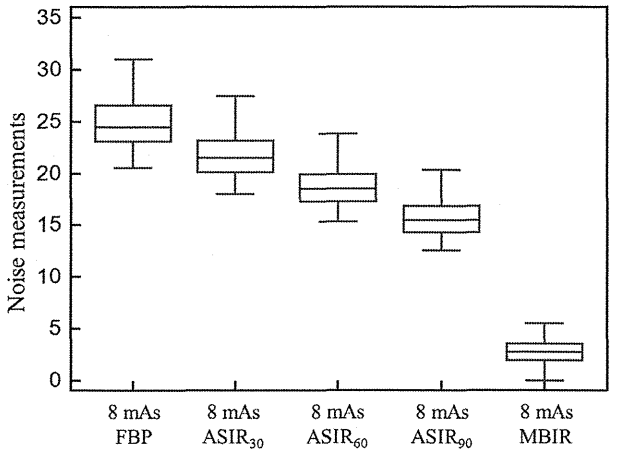

Figure 4. Quantitative noise measurements (mean ± standard deviation): 8-mAs FBP (24.7 ± 2.21), 8-mAs $ASIR_{30}$ (21.6 ± 2.01), 8-mAs $ASIR_{60}$ (18.5 ± 1.81), 8-mAs $ASIR_{90}$ (15.5 ± 1.64), and 8-mAs MBIR (2.71 ± 1.10). Significant differences in quantitative noise measurements were found among all groups ($P < .001$). ASIR, adaptive statistical iterative reconstruction; FBP, filtered back projection; MBIR, model-based iterative reconstruction.

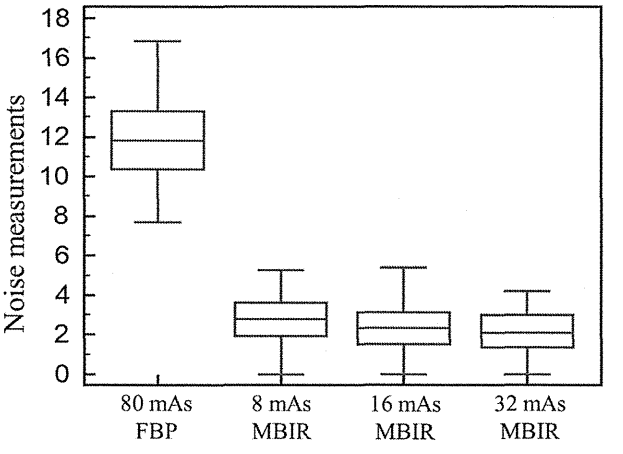

Figure 5. Quantitative noise measurements (mean ± standard deviation): 80-mAs FBP (11.99 ± 2.01), 8-mAs MBIR (2.73 ± 1.11), 16-mAs MBIR (2.42 ± 1.10), and 32-mAs MBIR (2.12 ± 1.10). Significant differences in quantitative noise measurements were found among all groups ($P < .001$). FBP, filtered back projection; MBIR = model-based iterative reconstruction.

observers impossible but did not adversely impact conspicuity or visibility of the CT findings evaluated in this study, namely central and peripheral airways and vessels, interlobar fissures, nodules, GGOs, and thickened interlobular septa. We did, however, observe obscuration of intralobular reticular opacities on MBIR images of one lung specimen with a "crazing paving" pattern because of diffuse alveolar hemorrhage. We postulate that visibility of these fine low-contrast abnormalities may be decreased on the ultra-low-dose MBIR images. Further research on diagnostic adequacy of low-dose MBIR images for broader spectrum of lung abnormalities including those of intrinsic low contrast is required before this technique can be adopted into routine clinical practice.

Although not possible in clinical patients, using this cadaveric lung model, we were able to perform multiple acquisitions to determine the minimum tube current–time product at which image quality of a low-dose MBIR study is comparable to that of a standard-dose FBP study. Of the three tube currents tested, 32-mAs MBIR images were rated highest with statistically significant improvements in conspicuity of each evaluated category of normal and abnormal CT findings, level of image noise, presence of streak artifact, and overall image quality. We found no significant difference in conspicuity of evaluated CT findings (GGOs, nodules, and interlobular septa) between 16-mAs MBIR as compared to 80-mAs FBP despite an 80% reduction in effective dose. At 90% dose reduction, significant decreases in overall image quality and conspicuity of interlobular septal thickening were observed on 8-mAs MBIR images. Thus, MBIR technique enables a submillisievert-dose (0.62 mSv) CT. This effective dose, which is well below the annual exposure from natural sources (3.1 mSv/year), is only 10 times greater than that delivered with two-view radiography (0.06 mSv for standard patient), including posteroanterior- and lateral-projection acquisitions (15,25).

Neroladaki et al. (14) have similarly reported limitations in detection of some CT findings on ultra-low-dose MBIR images that were acquired in their study at a radiation exposure (100 kVp, 6 mAs) similar to chest radiography. High-contrast lesions such as solid nodules and architectural distortion were consistently identified by three observers, while interobserver agreement for GGOs and emphysema were fair and poor, respectively.

Detectability of nodules on ultra-low-dose MBIR has been investigated by several groups (11,12,14). Using low-dose (50 mAs) FBP as the gold standard, Yamada et al. (12) report average true-positive fractions of 1.0 and 0.944 for calcified and ≥4 mm noncalcified nodules, respectively on ultra-low-dose (4 mAs) MBIR. Katsura et al. (11) compared 5-mAs MBIR to low-dose $ASIR_{50}$ and found no significant differences in detection of nodules ≥4 mm including nodules with nonsolid components; however, as compared to reference dose $ASIR_{50}$, only an average of 10.5 of 18 pure ground-glass nodules were identified on ultra-low-dose MBIR by the two observers.

Our study was limited by the small number of cases with only three types of abnormal CT findings included for formal evaluation; determination of the diagnostic adequacy of ultra-low-dose MBIR technique will require larger sample sizes with inclusion of a broader spectrum of representative lung CT findings that are encountered in clinical practice. The use of a cadaveric lung model did not allow us to evaluate the influence of a chest wall, body habitus, or motion artifacts on image quality. Moreover, histologic sections of cadaveric lungs should have been used to evaluate the fidelity of the various CT images. Because ASIR and MBIR algorithms are both manufactured by the same company, it is unclear as

to whether the results of our studies are applicable to other iterative reconstruction algorithms. Finally, although the image data sets used in the present study were randomized, perfect blinding to MBIR images might be difficult because it may be relatively easy to discriminate MBIR images with no concept of reconstruction algorithm from ASIR and FBP using a high–spatial-frequency algorithm.

In conclusion, ultra-low-dose thin-section CT images of the lung reconstructed using MBIR are of higher overall image quality with less noise and streak artifact than images reconstructed using ASIR. Even nearly 80% dose reduction under the use of MBIR does not degrade overall image quality.

REFERENCES

1. Prakash P, Kalra MK, Kambadakone AK, et al. Reducing abdominal CT radiation dose with adaptive statistical iterative reconstruction technique. Invest Radiol 2010; 45:202–210.
2. Singh S, Kalra MK, Hsieh J, et al. Abdominal CT: comparison of adaptive statistical iterative and filtered back projection reconstruction techniques. Radiology 2010; 257:373–383.
3. Honda O, Yanagawa M, Inoue A, et al. Image quality of multiplanar reconstruction of pulmonary CT scans using adaptive statistical iterative reconstruction. Br J Radiol 2011; 84:335–341.
4. Gervaise A, Osemont B, Lecocq S, et al. CT image quality improvement using Adaptive Iterative Dose Reduction with wide-volume acquisition on 320-detector CT. Eur Radiol 2012; 22:295–301.
5. Prakash P, Kalra MK, Ackman JB, et al. Diffuse lung disease: CT of the chest with adaptive statistical iterative reconstruction technique. Radiology 2010; 256:261–269.
6. Singh S, Kalra MK, Gilman MD, et al. Adaptive statistical iterative reconstruction technique for radiation dose reduction in chest CT: a pilot study. Radiology 2011; 259:565–573.
7. Funama Y, Taguchi K, Utsunomiya D, et al. Combination of a low-tube-voltage technique with hybrid iterative reconstruction (iDose) algorithm at coronary computed tomographic angiography. J Comput Assist Tomogr 2011; 35:480–485.
8. Moscariello A, Takx RA, Schoepf UJ, et al. Coronary CT angiography: image quality, diagnostic accuracy, and potential for radiation dose reduction using a novel iterative image reconstruction technique-comparison with traditional filtered back projection. Eur Radiol 2011; 21:2130–2138.
9. Thibault JB, Sauer KD, Bouman CA, et al. A three-dimensional statistical approach to improved image quality for multislice helical CT. Med Phys 2007; 34:4526–4544.
10. Katsura M, Matsuda I, Akahane M, et al. Model-based iterative reconstruction technique for radiation dose reduction in chest CT: comparison with the adaptive statistical iterative reconstruction technique. Eur Radiol 2012; 22:1613–1623.
11. Katsura M, Matsuda I, Akahane M, et al. Model-based iterative reconstruction technique for ultralow-dose chest CT: comparison of pulmonary nodule detectability with the adaptive statistical iterative reconstruction technique. Invest Radiol 2013; 48:206–212.
12. Yamada Y, Jinzaki M, Tanami Y, et al. Model-based iterative reconstruction technique for ultralow-dose computed tomography of the lung: a pilot study. Invest Radiol 2012; 47:482–489.
13. Vardhanabhuti V, Loader RJ, Mitchell GR, et al. Image quality assessment of standard- and low-dose chest CT using filtered back projection, adaptive statistical iterative reconstruction, and novel model-based iterative reconstruction algorithms. AJR Am J Roentgenol 2013; 200:545–552.
14. Neroladaki A, Botsikas D, Boudabbous S, et al. Computed tomography of the chest with model-based iterative reconstruction using a radiation exposure similar to chest X-ray examination: preliminary observations. Eur Radiol 2013; 23:360–366.
15. McCollough CH, Chen GH, Kalender W, et al. Achieving routine submillisievert CT scanning: report from the summit on management of radiation dose in CT. Radiology 2012; 264:567–580.
16. Markarian B, Dailey ET. Preparation of inflated lung specimens. In: Groskin SA, ed. Heitzman's The lung: radiologic-pathologic correlations. 3rd ed. St. Louis: Mosby, 1993; 4–12.
17. Aberle DR, Berg CD, Black WC, et al. The National Lung Screening Trial: overview and study design. Radiology 2011; 258:243–253.
18. Boehm T, Willmann JK, Hilfiker PR, et al. Thin-section CT of the lung: dose electrocardiographic triggering influence diagnosis? Radiology 2003; 229(2):483–491.
19. Goldman LW. Principles of CT: radiation dose and image quality. J Nucl Med Technol 2007; 35:213–225.
20. American Association of Physicists in Medicine. The measurement, reporting, and management of radiation dose in CT; 2008. Available at: http://www.aapm.org/pubs/reports/rpt_96.pdf. Accessed January 15, 2012.
21. Marin D, Nelson RC, Schindera ST, et al. Low-tube-voltage, high-tube-current multidetector abdominal CT: improved image quality and decreased radiation dose with adaptive statistical iterative reconstruction algorithm—initial clinical experience. Radiology 2010; 254:145–153.
22. Yanagawa M, Honda O, Yoshida S, et al. Adaptive statistical iterative reconstruction technique for pulmonary CT: image quality of the cadaveric lung on standard- and reduced-dose CT. Acad Radiol 2010; 17: 1259–1266.
23. Hara AK, Paden RG, Silva AC, et al. Iterative reconstruction technique for reducing body radiation dose at CT: feasibility study. AJR Am J Roentgenol 2009; 193:764–771.
24. Yu Z, Thibault JB, Bouman CA, et al. Fast model-based X-ray CT reconstruction using spatially nonhomogeneous ICD optimization. IEEE Trans Image Process 2011; 20:161–175.
25. Wall BF, Hart D. Revised radiation doses for typical X-ray examinations. Report on a recent review of doses to patients from medical X-ray examinations in the UK by NRPB. National Radiological Protection Board. Br J Radiol 1997; 70:437–439.